Robust Pressure-Actuated Liquid Metal Devices Showing Reconfigurable Electromagnetic Effects at GHz Frequencies

Brad L. Cumby, *Student Member, IEEE*, David B. Mast, Christopher E. Tabor, Michael D. Dickey, *Member, IEEE*, and Jason Heikenfeld, *Senior Member, IEEE*

***Abstract*—Pressure-actuated liquid metal devices are demonstrated for reconfigurable electromagnetic fundamentals at GHz frequencies, including tunable dipole antennas, switchable shielding with 35-dB attenuation, ∼30-dB polarizer attenuation, and ∼40° diffraction from a linear grating. In addition to a wide variety of electromagnetic effects, these devices are further advanced by: being highly physically flexible; in use of nontoxic GaInSn (68.5% Ga, 21.5% In, and 10.0% Sn) alloy as enabled by a sealed closed system with an acidic vapor background; and non-alloying/corrosion-resistant carbon inks for electrical connection. Collectively, this work addresses a wide variety of electromagnetic fundamentals, and the device construction advances required for real-world applications.**

***Index Terms*—Antennas, attenuation, diffraction, liquid metal, microfluidics, polarization, shielding.**

I. Introduction

HAVING multiple or reconfigurable electromagnetic capabilities within a single device is highly desirable, however, typical devices are limited in reconfigurability [1], [2] compared to actual physical re-arrangement of metal conductors to modify apertures, resonance lengths, etc. There is also increasing interest in physically flexible or conformal electronics [3], [4], which can improve user ergonomics and facilitate integration into applications where a rigid substrate is not possible. Furthermore, both reconfigurable and physically flexible electromagnetic devices combined could enable an array of applications that are not being envisioned by those pursuing either attractive attribute alone. Our working group and others have now shown that liquid metals can lead to significant reconfigurable [5]–[8], self-healing [9], and even stretchable devices [10], [11]. However, previous works have not examined a larger fundamental set of electromagnetic capabilities of fully sealed and reliable devices that bring experiment closer to application.

We report here an extension of our most recent work [12] involving pressure-actuated liquid metal devices (Fig. 1) with fundamental electromagnetic capabilities within the GHz regime spanning tunable dipole antennas, switchable shielding with 35-dB attenuation, ∼30-dB polarizer attenuation, and ∼40° diffraction from a linear grating. These devices consist

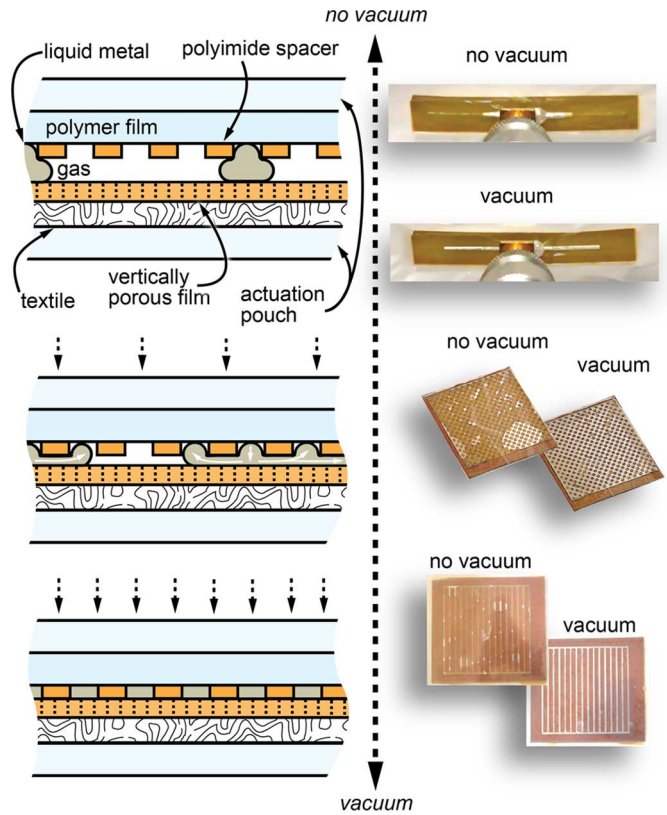


Fig. 1. Diagram of a reversible vacuum pressure-actuated liquid metal device (*left*) and photographed examples including antennas, shields, and polarizers (*right, top to bottom*).

Manuscript received October 22, 2014; revised January 30, 2015 and April 09, 2015; accepted July 25, 2015. Date of publication August 28, 2015; date of current version October 02, 2015. The work of B. L. Cumby, D. B. Mast, and J. Heikenfeld was supported by the Air Force Research Laboratory under Contract UES-875-060-020 and by the Southwestern Ohio Council for Higher Education. The work of M. D. Dickey was supported by the National Science Foundation (NSF) under CAREER Award CMMI-0954321. This paper has supplementary downloadable material available at http://ieeexplore.ieee.org, provided by the authors. This includes a PDF document, containing a figure and measured, simulated, and calculated data. This material is 189 kB in size. *(Corresponding author: Jason Heikenfeld.)*

B. L. Cumby and J. Heikenfeld are with the Department of Electrical Engineering and Computing Systems, University of Cincinnati, Cincinnati, OH 45221 USA (e-mail: heikenjc@ucmail.uc.edu).

D. B. Mast is with the Department of Physics, University of Cincinnati, Cincinnati, OH 45221 USA.

C. E. Tabor is with the Materials and Manufacturing Directorate, Air Force Research Laboratory, Wright Patterson, OH 45433 USA.

M. D. Dickey is with the Department of Chemical and Biomolecular Engineering, North Carolina State University, Raleigh, NC 27695 USA.

Color versions of one or more of the figures in this paper are available online at http://ieeexplore.ieee.org.

Digital Object Identifier 10.1109/TMTT.2015.2470244

0018-9480 © 2015 IEEE. Personal use is permitted, but republication/redistribution requires IEEE permission.
See http://www.ieee.org/publications_standards/publications/rights/index.html for more information.

of inherently flexible materials, use nontoxic GaInSn (68.5% Ga, 21.5% In, and 10.0% Sn) alloy, employ nonalloying/corrosion-resistant electrodes, and are implemented in a sealed closed system with oxide-preventing acidic vapor background. In this paper, firstly, details are provided on novel device attributes spanning from basic materials to system-level design. Next, each electromagnetic demonstration is discussed in detail, one-by-one, including unique device aspects, experimental results, and comparison to theoretically modeled behavior. Although the devices in this work are specifically designed for the GHz regime, geometrical scaling and design allowing for predicted droplet size and placement [13] can lead to a wider range of applications ranging from MHz to THz. With fundamental capabilities now demonstrated, and requisite device construction better understood, the utility of these liquid metal devices can be more broadly and accurately envisioned for real-world applications.

II. Device and System-Level Design

While the basic physics of the pressure-actuation method used for the liquid metal devices is reviewed here, a more detailed description can be found elsewhere [5]. The devices all rely on a similar construction (Fig. 1), while utilizing competitive liquid metal shaping with Laplace and vacuum pressures. With $<$10 pounds per square inch (psi) vacuum applied to two flexible films, one film having a network of microreplicated trenches (between spacers), the Laplace pressure [14] outside the trenches increases, driving the liquid metal into the trenches (lower Laplace pressure). This increase in Laplace pressure originates from the vacuum collapse of the channel height between the films, reducing the radius of curvature of the liquid metal residing between these two films (Laplace pressure is inversely proportional to the radius of curvature for a liquid surface) [5]. Upon release of vacuum, the channel height returns to its original position, erasing the liquid metal pattern as surface tension dewets the liquid metal into droplets that compacts to 10–100$\times$ less area than when in the trenches. It should be noted that the thickness of the liquid metal was not measured in this actuated state it is assumed that the thickness is equal to that of the trenches into which the liquid metal is driven.

Our previous work [5] used Hg as the liquid metal, which is less desirable than liquid GaIn or GaInSn in terms of toxicity. However, these alloys are sensitive to low amounts of oxygen ($>$1 ppm [15]) forming an oxide layer that renders the liquid metal unreconfigurable. Our solution is to instead utilize a closed system (Fig. 2) that allows the reconfiguration of liquid metal devices by differential pressures and eliminating the concern of oxidation. This new system has three main components [see Fig. 2(a)]: an actuation pouch, $\sim$ 75 μm in thickness, containing both a device and an acid soaked patch (textile $\sim$100 μm in thickness), a recirculating pump (Parker H119-11), and a storage pouch also containing an acid soaked patch. The actuation pouch serves two purposes, which are: 1) to provide a protective barrier against the ambient oxygen that would otherwise oxidize the liquid metal and 2) to provide a seal so that a vacuum can be created within the pouch and therefore provide an differential actuation pressure up to approximately 1 atm

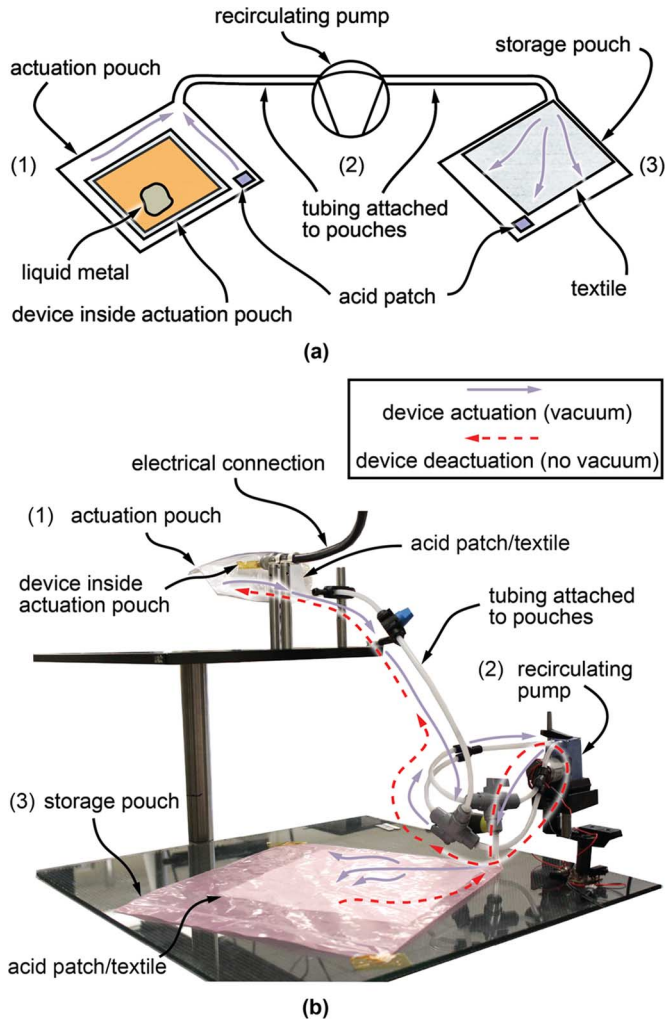


Fig. 2. (a) Diagram and (b) testing setup, photograph of the system used for the experiments shown herein. The system is easily miniaturized (not shown).

($\sim$10 psi). The pump accomplishes these functions by allowing for a reversible transition between evacuated and nonevacuated states of the actuation pouch, as well as recirculating acid vapor sourced from the acid-soaked (hydrochloric acid) textile ($\sim$0.12-mL liquid). It should be noted that the volume of the acid can be decreased as well as the acid diluted (0.1 M); however, the process of removing the oxide will take longer. The acid vapor rids the metal of oxide in a closed system, simplifies experimentation, and improves reliability as compared to a system that would require a more robust seal and filled with only inert gas. Although demonstrated as a bench-top setup, the system could be easily incorporated in a miniaturized portable design.

For the actual devices inside the actuation pouch, the basic cross section is shown in Fig. 1. The polymer film carries a polyimide spacer, which defines the inverse of the liquid metal pattern in the vacuum (actuated) state. The vertically porous film is a track-etched polyimide membrane (AR Brown-US, 3M101200250, 200 $\times$ 250 mm) with a pore (1-μm diameter) density of 2.2 $\times$ 10^7cm^{-2}, and 30 μm in thickness that allows gas transport, but with pore radii that are so small that the liquid metal is unable to wet into the pores due to Laplace

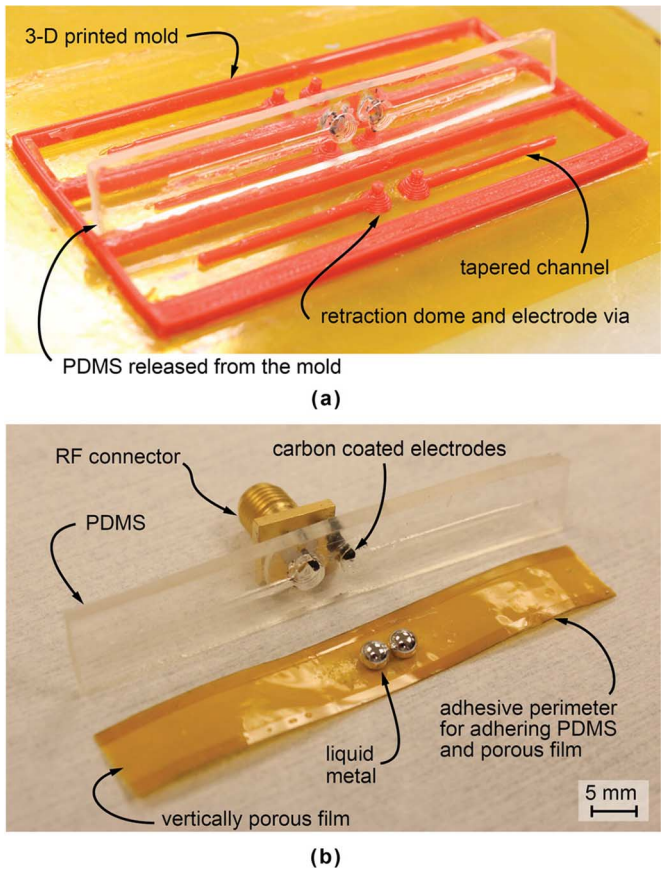


Fig. 3. (a) Mold utilized for casting PDMS consisting of a tapered channel, retraction dome, and electrode via. (b) Components of the device right before final assembly.

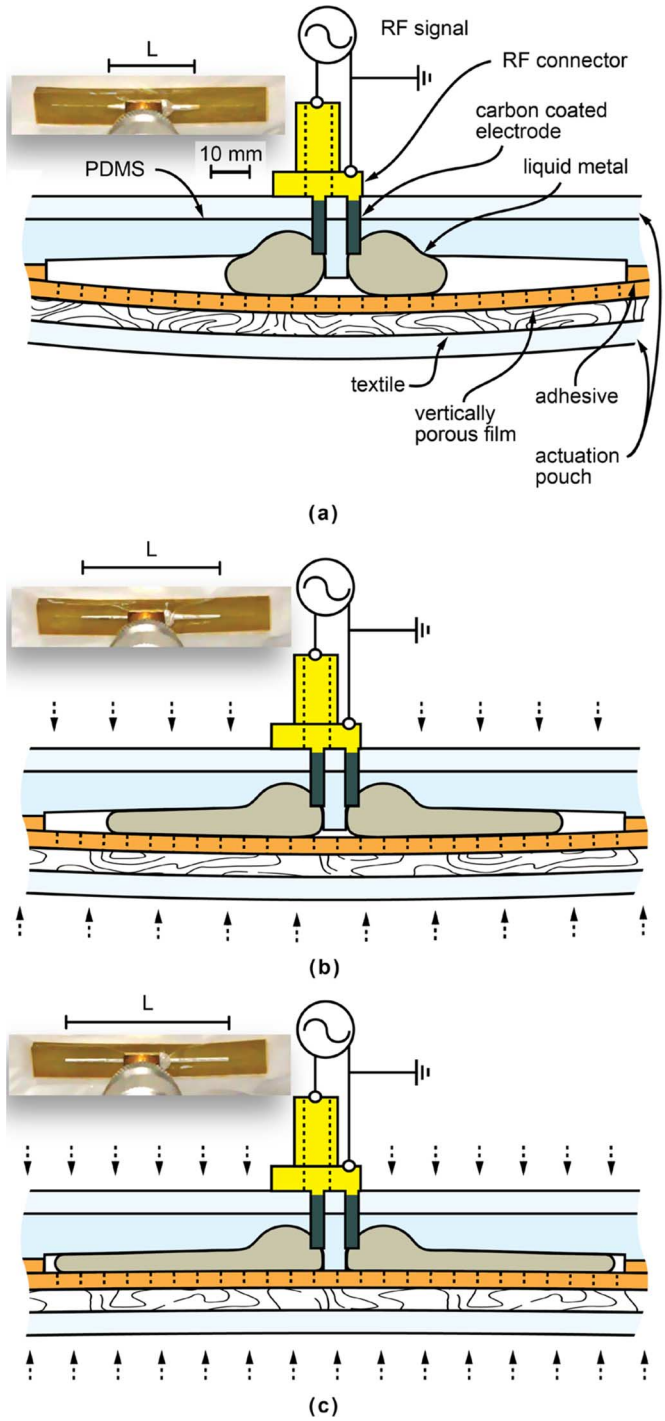


Fig. 4. Dipole operation diagrams and experimental photographs including labeling of the combined dipole length (L). (a) No vacuum. (b) Partial vacuum pressure. (c) Full vacuum pressure.

pressure. The textile is added simply to enable more rapid horizontal transport of gas into and out of the device. For each particular device demonstration, there are some device modifications, which are now discussed in detail.

III. Tunable Dipole Antenna

A. Dipole Design and Fabrication and Setup

A tunable dipole antenna was assembled using components shown in Fig. 3. The polydimethylsiloxane (PDMS) superstrate, 2.2 mm in thickness, was formed using Dow Corning Sylgard 184 and has a specific geometry for promoting analog control of the liquid metal actuation (more pressure results in an equal increase in length of each dipole arm Fig. 4). There are two key design features. Firstly, to maintain contact between that of the liquid metal and the RF connector electrodes, at the electrode tips there is also a retraction dome in the PDMS that creates a larger cavity that the liquid metal will always wet into because of minimum Laplace pressure (Figs. 3 and 4). Secondly, the channel that the PDMS is driven into with vacuum actuation is tapered to promote retraction of the liquid metal without splitting into satellite droplets [16] and to allow analog control (liquid metal dipole length increases with vacuum level). To create such a tapered channel topography, we utilized simple 3-D printing (MakerBot Replicator 2) to make the casting mold for the PDMS.

To provide RF electrode connections that are nonalloying with the liquid metal, a conductive carbon ink protective coating was added (Henkel, Acheson Electrodag PF-407C). The legs of an RF SMA connector were dipped into the carbon ink and baked at 120 °C for 15 min. The coated RF electrode tips were then inserted through two vias that were laser ablated through the device pouch as well as placed through the

vias formed in the PDMS superstrate. Lastly, the adhesive perimeter (Figs. 3 and 4) was achieved using 101.6-μm-thick double-sided polyimide adhesive tape (Kapton). Two liquid metal droplets were dosed under the retraction domes and then the superstrate pressed against the adhesive layer. The device is then placed into the actuation pouch. The RF connector is connected to a coaxial cable, which is then connected to a network analyzer (Agilent 8753D).

B. Dipole Theory and Results

A dipole as shown in Fig. 4 is tunable in terms of the dipole length and therefore a tunable frequency (f) resonance. Being that the dipole antenna arm length is tunable (via applied vacuum pressure), this resonance peak will be tunable, and is approximated by a dielectrically loaded dipole antenna by

$$f = \frac{c}{2 * L\sqrt{\varepsilon_{\text{eff}}}} \tag{1}$$

where c is the speed of light, L is the length of the dipole (Fig. 4), and the effective dielectric, ε_{eff}, is a combination of the permittivities of the surrounding polymers. The effective permittivity used in (1) is $\varepsilon_{\text{eff}} \sim 2.0$.

As can be seen, the experimentally measured data (network analyzer), calculated data (1), and simulated data (COMSOL) are shown in Fig. 5. Although COMSOL was used to simulate the experimental setup in 3-D involving electromagnetics, only one could simulate the mechanical deformation in conjunction with electromagnetics. Several finer observations are worth mentioning. The dipole data shown in Fig. 5 shows that starting at $\sim$3.5 GHz the response is ~ -10 dB throughout the measured frequency range. This response is believed to be due to several facts. One is that a balun was not used and that there is coupling to nearby metallic objects such as a stage that a cable mount is attached to, as seen in Fig. 2(b). Also although there is a gap in resonant frequencies shown between points 40 and 21 mm of Fig. 2(a), the length and tunability is indeed continuous between these points. However, the resonant frequencies shown were chosen to demonstrate that the resonant frequency can be controlled in fine increments (45–40 mm), as well as broad increments (40–21 mm). While some resonant data is not shown in Fig. 5 for simplicity, it can be seen in the supplementary material.[1]

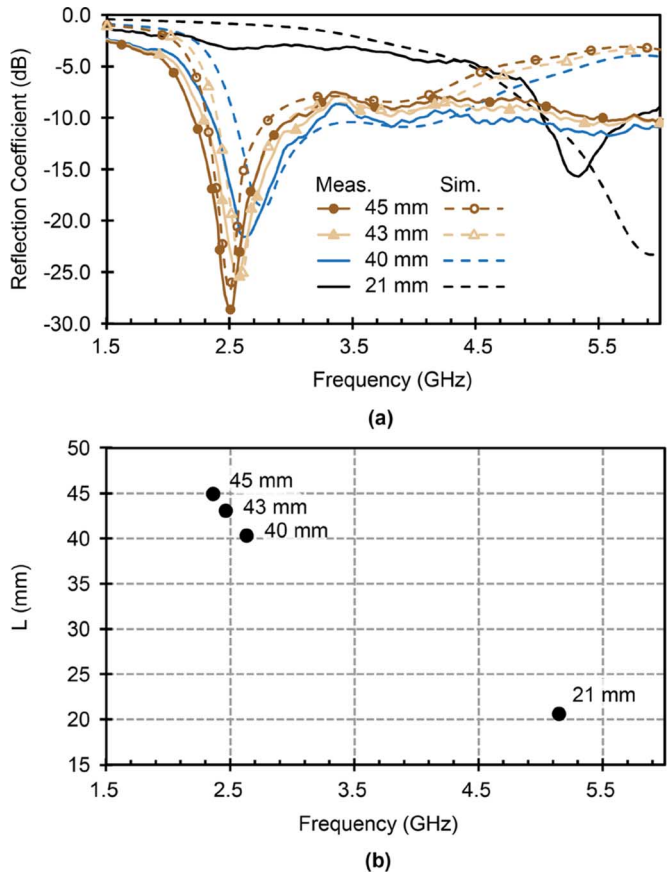


Fig. 5. Dipole device data as vacuum pressure is applied and dipole length is varied as: (a) measured, simulated (COMSOL), and (b) calculated.

IV. Switchable Shield

A. Shield Design and Fabrication and Setup

A switchable electromagnetic shield (Fig. 6) was created using flexible materials similar to those shown in the diagrams of Fig. 1. The laser-ablated polyimide spacers of the shield were $\sim$0.9 mm in diameter, 50 μm in thickness, spaced center-to-center at 3.0 mm in an irregular hexagonal lattice, and carried by a polyethylene terephthalate (PET) substrate 254 μm in thickness. Like the dipole antenna, a double-sided Kapton tape adhesive boarder was used to seal the substrate carrying the polyimide spacers to the vertically porous film. The sealed device was placed on top of a textile and then placed inside the actuation pouch. The transmission of the device was measured using a standard rectangular waveguide (WR-284) that contains an iris at each end. These irises form a resonant cavity within the waveguide to allow incoming microwaves of discrete frequencies to pass through to a power meter attached to one end of the waveguide. The shield is placed over the iris at the entrance of the waveguide opposite to the power meter. Microwaves are incident upon the setup, transmitting through each component: first the shield, the entrance iris, the waveguide, the second iris, and finally to the power meter. The power is measured as the device is transitioned from the nonactuated to the actuated state. This same process was repeated for another standard rectangular waveguide (WR-90) setup, except that the sample was placed between two horn adaptors attached to the end of the transmitting and receiving waveguides [see Fig. 8(b)].

B. Shield Theory and Results

The switchable shield reconfigures between multiple compact droplets to a reticulated network that attenuates incoming microwaves. In a droplet form, in the nonactuated state, the liquid metal only slightly impedes the incoming microwaves as they pass through the device to the power meter; however, in the actuated state, the liquid metal spreads through the space formed between adjacent spacers making a reticulated network and further attenuating the microwaves. The transmission loss

[1]Supplemental material for the reader can be downloaded online at http://ieeexplore.ieee.org/

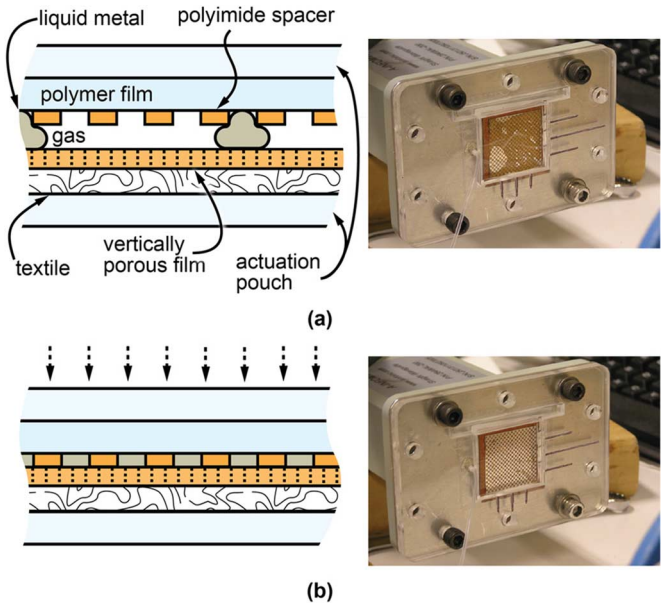


Fig. 6. Shield operation diagrams (*left*) and experimental photographs (*right*). (a) No vacuum. (b) Full vacuum pressure.

or shielding effectiveness (S.E.) of the shield was approximated using [17],

$$\text{S.E.} = 20\log\left(\frac{3ab\lambda_0}{2\pi d^3}\right) + \frac{32t}{d} - 20\log\left(\frac{1}{\cos\theta_i}\right) \quad (2)$$

$$b = a/2\tan\theta \quad (3)$$

where a is the spacing from center to center of the apertures (polyimide spacers), θ is a 45° angle between rows of apertures, d is the diameter of the spacers, θ_i is the incident angle of the microwaves, λ_0 is the free-space wavelength, and t is the thickness of the shield. It should be noted that the insertion loss of the device in the off state was measured to be 3.5 dB for the S.E. measurements. The data shown in Fig. 7(a) and (b) shows the amount of power measured in both actuated and nonactuated states of the shield. The simulated data in Fig. 7(c) is completed by using a 2-D simulation (COMSOL) of the shield setup with only one row of liquid metal/polyimide spacers as a unit cell. The results were then modified according to [18]

$$\text{S.E.}_{\text{net}} = \text{S.E.(simulated)} - 20\log\left(\sqrt{n}\right) \quad (4)$$

where n is the largest number of consecutive apertures formed in a straight line within an array of total length that is less than half a wavelength.

The shield data shown in Fig. 7 varies as a function of frequency, but not in a way that is normally predicted by a conventional shielding equation (shielding steadily decreases as a function of frequency). In regard to the WR-284 waveguide setup, since the shield covers the iris with a new conductive boundary this may cause the resonator at certain frequencies to be more/less efficient due to the reflections from the face of the shield (shifted resonance, decreasing the shielding during certain frequencies). With the WR-90 setup this change in shielding could be due to the waveguide setup when the space between the shield and the iris at the entrance of the waveguide also forms a

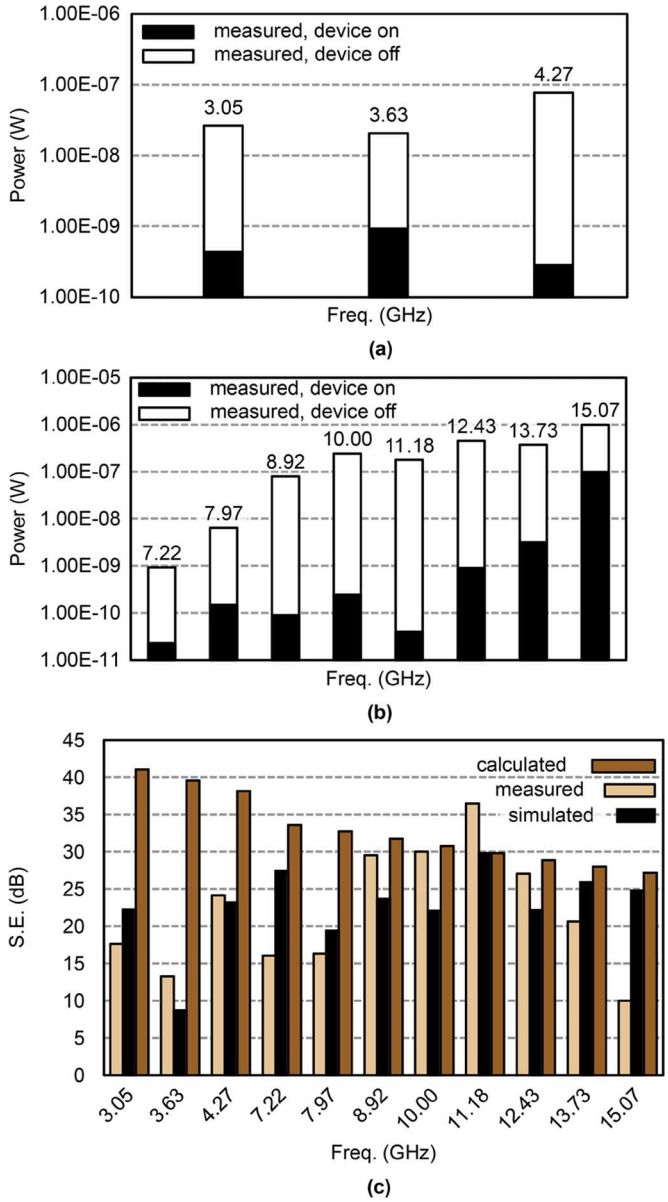


Fig. 7. (a) and (b) Measured power attenuation of the switchable shield in on and off states. (c) Calculated, measured, and simulated (COMSOL) results of the switchable shield. (a) WR-284 setup frequency transmission data. (b) WR-90 setup frequency transmission data. (c) S.E. WR-284 and WR-90 setup.

standing wave at different frequencies (see simulation, Fig. 8). Being that the WR-90 setup involved the horn adapters to remain in close proximity to the shield or in the near-field will account for some differences in the theory versus measured due to the fact that the theory assumed a far-field situation. This will lead to a discrepancy in the impedance, and therefore, a difference in impedance matching or S.E.

V. Switchable Polarizer

A. Polarizer Design and Fabrication and Setup

A switchable electromagnetic polarizer (Fig. 9) was fabricated similar to the shield device, but with linear spacers of 0.94-mm width, 100-μm height, 43.0-mm length, and spaced 1.673 mm apart. The transmission of the polarizer is measured

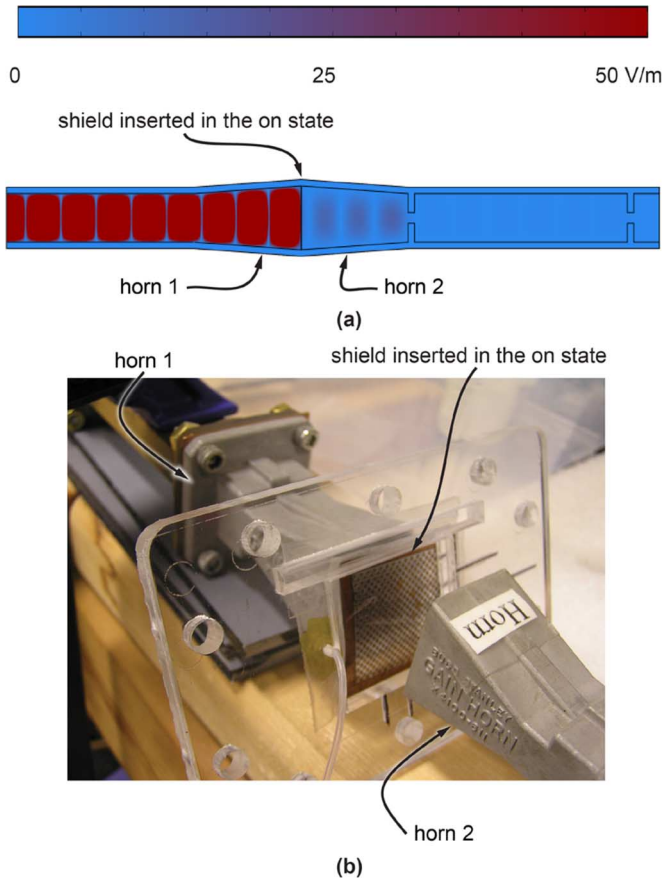


Fig. 8. Simulation: (a) of shield in WR-90 setup displays strong resonance resulting in a potential decrease in S.E. in (b), which is the associated experimental setup (horn adaptors are slightly separated for photograph purposes, but not during experiment). (a) Simulation of transmission at 11.18 GHz. (b) Testing setup.

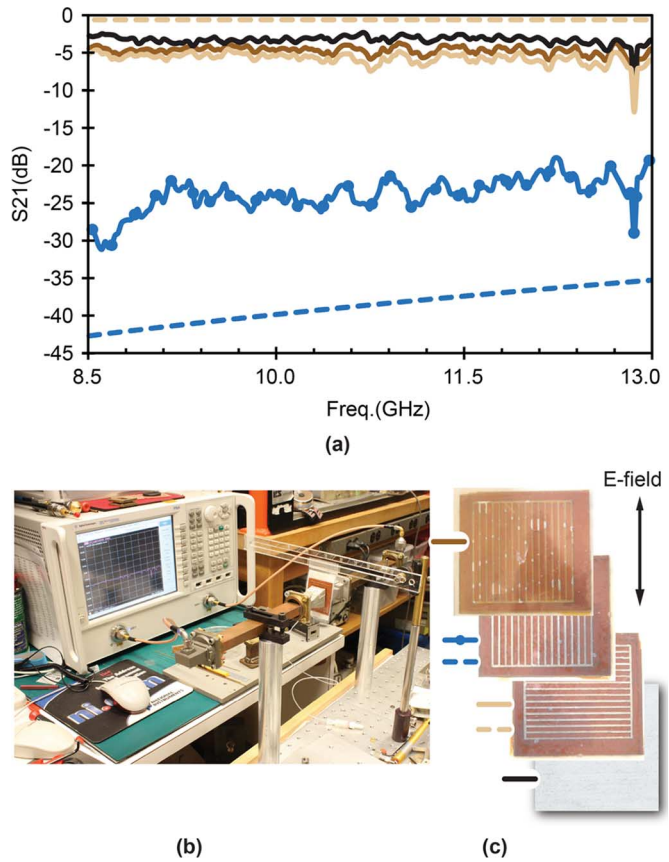


Fig. 9. Polarizer measured and calculated results as the device is in different orientations (with respect to the microwave polarization) and device actuation states. See inset with legend (c), from top to bottom: parallel/off state (measured); parallel/on state (measured) (calculated); perpendicular/on state (measured) (calculated); no device inserted (measured). (a) Measured and calculated data. (b) Testing setup. (c) Inset with legend.

using a WR-90 waveguide setup involving two separate straight sections of waveguide each having a standard gain horn attachment, as shown in Fig. 9(b). The polarizer is placed between the two horn attachments and transmission is measured as microwaves begin to pass through one of these horn/waveguide sections, through the polarizer sample, and then into the opposing horn/waveguide to the power meter. The transmission is measured as the polarizer is in the on state as well as in the off state, and again measured when the polarizer is rotated 90° with respect to the incoming microwave polarization. In the off state, the polarizer only slightly impedes these microwaves, whereas in the on state the metallic lines formed between the standoffs will then reflect and absorb aligned polarizations (E-field parallel to the metallic lines) and transmit the nonaligned polarization (E-field perpendicular to the metal lines).

B. Polarizer Theory and Results

The polarizer reconfigures between multiple compact droplets to metallic lines. In a droplet form, in the nonactuated state, the liquid metal only slightly impedes the incoming microwaves as they pass through the device to the power meter; however, in the actuated state, the liquid metal spreads throughout the space formed between adjacent spacers making a network of metallic lines and attenuating the microwaves based upon the orientation of the lines relative to the incoming microwaves. The coefficients of transmission for parallel and perpendicular orientations relative to the incoming electric field can be approximated by [19]

$$T_{||} = \frac{k^2 d^2 \ln^2\left[\sin\frac{\pi a}{d}\right]/\pi^2}{1 + k^2 d^2 \ln^2\left[\sin\frac{\pi a}{d}\right]/\pi^2} \tag{5}$$

$$T_{\perp} = \frac{1}{1 + k^2 d^2 \ln^2\left[\cos\frac{\pi a}{d}\right]/\pi^2} \tag{6}$$

where k is the propagation constant $2\pi/\lambda$, a is the width of the metallic lines, and d is the spacing between adjacent metallic lines. The transmission loss of the calculated and measured results, waveguide setup, and experimental images are shown in Fig. 9. When referring to Fig. 9(a) (top to bottom), it can be seen the calculated data for the device in the perpendicular position should transmit almost all the incoming electric field, as the transmission loss is ~ 0 dB. The measured results of the setup with no device inserted, the device inserted in the off state, as well as the device inserted in the perpendicular/on state are shown directly below the calculated data. As can be seen, there is slight attenuation already with no device inserted. This is most likely due to the fact that the transmitting and receiving waveguide sections on either side of the device are close

(near-field) to each other. The alignment of the two waveguides is not ideal and can cause a slight loss in transmission as well. Although there is a deviation, it is only slight and could be decreased if the distance as well as alignment were optimized. The last two sets of data are the measured and calculated results when the device is in the on state and oriented parallel to the E-field. Although there is a larger deviation between this set of data, the trend is approximately parallel (transmission loss decreases as Freq. increases). This deviation is attributed to the fact that the calculations used herein are under the assumptions that the metal is a perfect conductor and the wave is propagating in free space. As mentioned above, the experiment is in the near-field zone. Also, the metal is not a perfect conductor ($\sigma \sim 0.38 \times 10^7$ S/m), which will affect the reflection/coupling and therefore the transmission.

VI. Switchable Electromagnetic Diffraction Grating

A. Grating Design and Fabrication and Setup

A switchable electromagnetic diffraction grating (Fig. 10) is reported using flexible materials such as polyimide and PET, similar in construction to the polarizer of the previous section. The superstrate consists of a planar PET sheet measuring 254 μm in thickness, and carrying linear polyimide spacers (laser ablated Kapton tape) measuring 4.0 mm in width, 0.73 mm in spacing, 50 μm in thickness, and 43.0 mm in length. Double-sided polyimide adhesive tape (Kapton, 101.6 μm thick) was placed onto a 30-μm-thick track etched polyimide membrane and ablated so that a square adhesive border remained. The liquid metal was dosed on top of the polyimide spacers. To make a complete seal, the polyimide membrane was placed over top of the liquid metal and pressed against the PET substrate. The sealed device is placed on top of a textile and placed inside the actuation pouch. The device is then placed into a 100-GHz transmission setup to measure diffraction. The setup consists of two horns, one of which is a transmitting antenna and the other is a horn that is placed onto a swing arm that measures the incoming microwave signal as a function of diffraction angle. The device is placed onto the face of the transmitting horn. The receiving horn was connected to a fluke meter to measure the voltage induced by the incoming microwave signal for the actuated and nonactuated states, as the rotation of the receiver was incremented.

B. Grating Theory and Results

A diffraction grating shown in Fig. 10(b) (inset) reconfigures from multiple compact droplets to metallic lines. While in droplet form, the microwaves are slightly impeded, and in linear form, the microwaves is diffracted and was calculated by the well-known equation

$$d \sin \theta = m\lambda \tag{7}$$

where d is the center-to-center distance of the spacing between adjacent metallic lines, θ is the angle between the central maximum and the maximum at the order m, m is the nth maximum, and λ is the wavelength of the source. The calculated angle for the first-order maximum is 40°. The measured diffractive data is shown in Fig. 10. As can be seen, the first maximum is in close agreement to the expected 40°. However, there are dips in the central maximum as well as variance in the widths of the first maxima. This is most likely due to the imperfect filling of the channels with liquid metal, as well as the undesired displacement of liquid metal into the region outside the channels.

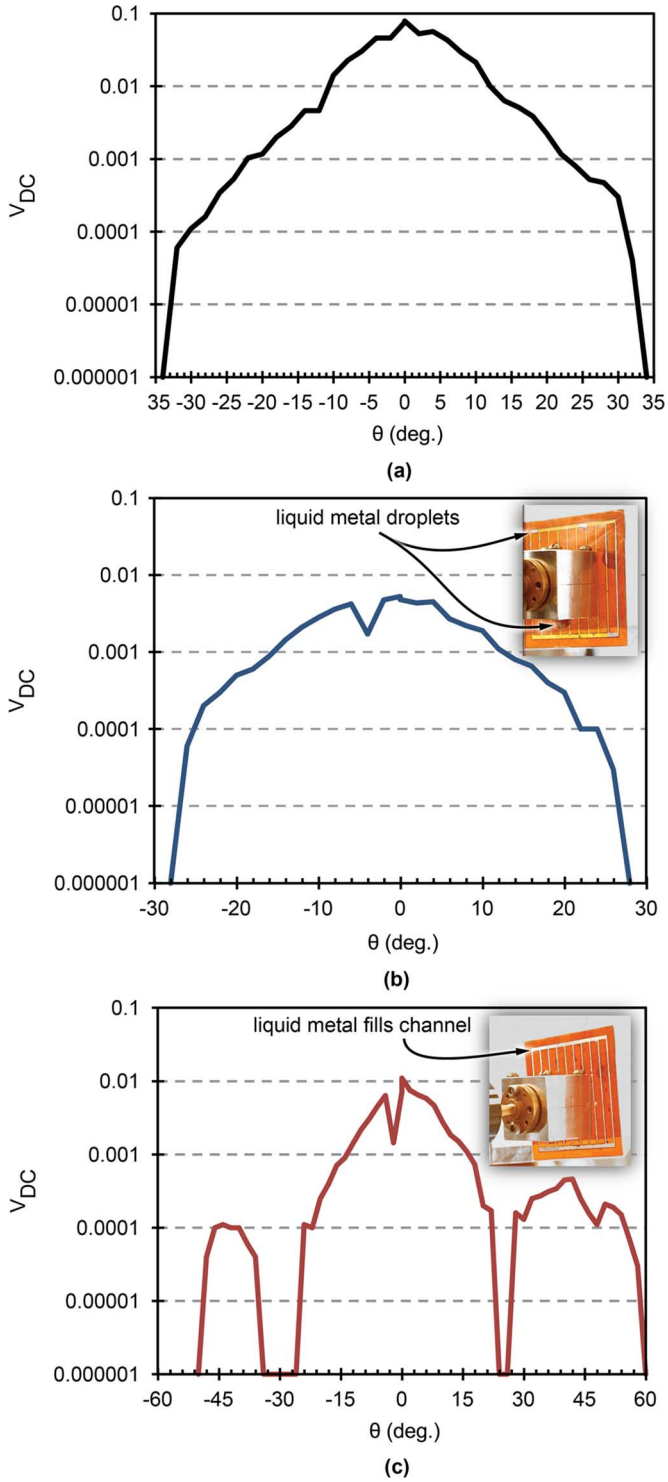


Fig. 10. Measured diffractive results as a function of angle of the diffraction grating setup and their associated experimental photos when: (a) no device is inserted, (b) the device is inserted in the off state, and (c) the device is inserted in the on state.

VII. Discussion

Although the switching lifetime of this system was not tested, it will be limited by leakage/diffusion of the acidic vapor, which is utilized in this approach to maintain the fluidic properties of the gallium alloy by reacting with the native surface oxide. This can be mitigated with thin film diffusion barriers. The switching rate will be highly dependent on the device geometry, generally related to the distance between the two extreme cases of actuation, but will also be dependent on the microchannel geometry, interfacial energies at the liquid metal and the channels surfaces, and the pressures applied to drive the metal. While this rate is not investigated in this paper, the authors have previously reported experimental validation of actuation speeds exceeding 30 cm/s [5]. The stability of these devices with respect to motion and vibration was not tested, however, traditional microfluidic approaches such as Laplace pressure threshold barriers or posts could be used to limit the instabilities brought about by either of these stimuli. These barriers could replace solid areas, i.e., the spacing between adjacent metallic lines of devices such as the shield, polarizer, and grating shown in this work to provide a tunability of spacing/width with input pressure, as shown in work by Khan *et al.* [6]. Although the work in [6] is irreversible, it complements the work reported herein and if both were used in conjunction would provide tunable effects that would then be reversible. Using previous reconfigurable/tunable approaches involving parasitic coupling or pressure as in [20] and [21], respectively, one has to account for the change in reconfiguration of the liquid metal to maximize parasitic coupling, use device real-estate due to parasitic components, and limit reconfigurability by using minute displacements of the liquid metal. Using the proposed reconfiguration scheme reported herein while utilizing the aforementioned techniques in [6], one could take full advantage of the reconfigurable medium being liquid to maximize reconfigurability. In this case, when transitioning from a compact form (semi-spherical droplet) to a shape with much larger surface area, as reported in the authors' previous work [5], the shape reconfiguration range would be large. Without relying on coupling of parasitics and the placement thereof, this large contrast in surface area will allow for larger electromagnetic tunability while keeping the device compact. Power handling should also be of interest in future work as it has been investigated in [22] for mercury, however, as the authors in this work mention, packaging of liquid metal devices will be pertinent to understanding power handling, especially with gallium alloys where an oxide presents technical challenges. While the thermal expansion of these gallium alloys may be considered, the effect should be minimal due to a spatial expansion coefficient of $11.5 \times 10 - 5$ [23]. Finally, it should be noted that the losses due to the reduced conductivity compared to copper of the liquid metal should be considered when appropriate. This may have an impact on efficiency, as discussed and measured in [24] depending on the device and concentration of electric fields.

VIII. Conclusion

Reported herein were pressure-actuated liquid metal devices with fundamental electromagnetic capabilities within the GHz regime spanning tunable dipole antennas, switchable shielding with 35-dB attenuation, $\sim$ 30-dB polarizer attenuation, and $\sim 40^{\circ}$ diffraction from a linear grating. This work solves real-world challenges with a complete system-level design including: nontoxic GaInSn (68.5% Ga, 21.5% In, and 10.0% Sn) alloy; employing nonalloying/corrosion-resistant electrodes; a closed system with oxide-preventing acidic vapor background. Experimental data for devices was coupled with theoretical calculations, which confirms that all devices can be specifically designed and perform as expected for various reconfigurable electromagnetic applications. In conclusion, this work provides both the theoretical evidence and the applied breakthroughs needed for real-world application of reconfigurable liquid-metal electromagnetic devices.

References

[1] F. B. Gross, "Reconfigurable antennas," in *Frontiers in Antennas: Next Generation Design and Engineering*. New York, NY, USA: McGraw-Hill, 2011, pp. 277–703.

[2] S. Mazlouman, A. Mahanfar, C. Menon, and R. Vaughan, "Mechanically reconfigurable antennas using electro-active polymers (EAPs)," in *IEEE Int. Antennas Propag. Symp.*, Spokane, WA, USA, 2011, pp. 742–745.

[3] R. Kim *et al.*, "Waterproof AlInGaP optoelectronics on stretchable substrates with applications in biomedicine and robotics," *Nature Mater.*, vol. 9, no. 11, pp. 929–937, Nov. 2010.

[4] T. Someya, "Flexible electronics allow us to cover robots and humans with stretchy sensors," *IEEE Spectr.*, vol. 50, no. 9, pp. 50–56, Sep. 2013.

[5] B. Cumby *et al.*, "Reconfigurable liquid metal circuits by Laplace pressure shaping," *Appl. Phys. Lett.*, vol. 101, no. 17, pp. 174102–174102-5, Oct. 2012.

[6] M. Khan, G. Hayes, J. So, G. Lazzi, and M. D. Dickey, "A frequency shifting liquid metal antenna with pressure responsiveness," *Appl. Phys. Lett.*, vol. 99, no. 1, pp. 013501–013501-3, Jul. 2011.

[7] Y. Damgaci and B. Cetiner, "A frequency reconfigurable antenna based on digital microfluidics," *Lab on a Chip*, vol. 13, no. 15, pp. 2883–2887, 2013.

[8] J. So *et al.*, "Reversibly deformable and mechanically tunable fluidic antennas," *Adv. Funct. Mater.*, vol. 19, no. 22, pp. 3632–3637, Nov. 2009.

[9] E. Palleau, S. Reece, S. Desai, M. Smith, and M. D. Dickey, "Self-healing stretchable wires for reconfigurable circuit wiring and 3D microfluidics," *Adv. Mater.*, vol. 25, no. 11, pp. 1589–1592, Mar. 2013.

[10] J. Park *et al.*, "Three-dimensional nanonetworks for giant stretchability in dielectrics and conductors," *Nature Commun.*, vol. 3, no. 3, pp. 916–923, Jun. 2012.

[11] S. Zhu *et al.*, "Ultrastretchable fibers with metallic conductivity using a liquid metal alloy core," *Adv. Funct. Mater.*, vol. 23, no. 18, pp. 2308–2314, May 2013.

[12] B. Cumby, D. Mast, C. Tabor, M. Dickey, and J. Heikenfeld, "Robust pressure-actuated liquid metal devices showing reconfigurable electromagnetic effects at GHz frequencies," in *IEEE Int. Antennas Propag. Symp.*, Jul. 6–11, 2014, pp. 553–554.

[13] R. Zhao, B. Cumby, A. Russell, and J. Heikenfeld, "Large area and low power dielectrowetting optical shutter with local deterministic fluid film breakup," *Appl. Phys. Lett.*, vol. 103, 2013, Art. ID 223510.

[14] J. Berthier, *Micro-Drops and Digital Microfluidics*, 2nd ed. Norwich, NY, USA: William Andrew, 2008, vol. 1, pp. 19–34, no. 1.

[15] T. Liu, P. Sen, and C. Kim, "Characterization of nontoxic liquid-metal alloy galinstan for applications in microdevices," *J. Microelectromech. Syst.*, vol. 21, no. 2, pp. 443–450, Apr. 2012.

[16] R. Ahmed and T. Jones, "Optimized liquid DEP droplet dispensing," *J. Micromech. Microeng.*, vol. 17, no. 5, pp. 1052–1058, May 2007.

[17] T. Otoshi and K. Woo, "Further studies of microwave transmission through perforated flat plates," JPL, Pasadena, CA, USA, Deep Space Netw. Progress Rep. Sep. and Oct. 1971, Dec. 1971, vol. 6, pp. 125–129.

[18] H. W. Ott, "Apertures," in *Electromagnetic Compatibility Engineering*. New York, NY, USA: Wiley, 2009.

[19] H. Lamb, "On the reflection and transmission of electric waves by a metallic grating," in *Proc. Lond. Math. Soc.*, London, U.K., 1898, vol. 29, pp. 523–540.

[20] D. Rodrigo, L. Jofre, and B. A. Cetiner, "Circular beam-steering reconfigurable antenna with liquid metal parasitics," *IEEE Trans. Antennas Propag.*, vol. 60, no. 4, pp. 1796–1802, Apr. 2012.
[21] W. M. Zhu *et al.*, "Metamaterial tunable filter with liquid metal," in *IEEE 26th Int. Microelectromech. Syst. Conf.*, Jan. 20–24, 2013, pp. 725–728.
[22] P. Sen and C.-J. Kim, "A fast liquid-metal droplet microswitch using EWOD-driven contact-line sliding," *J. Microelectromech. Syst.*, vol. 18, no. 1, pp. 174–185, Feb. 2009.
[23] M. Knoblauch, J. M. Hibberd, J. C. Gray, and A. Van Bel, "A galinstan expansion femtosyringe for microinjection of eukaryotic organelles and prokaryotes," *Nature Biotechnol.*, vol. 17, pp. 906–909, Sep. 1999.
[24] G. J. Hayes, S. Ju-Hee, A. Qusba, M. D. Dickey, and G. Lazzi, "Flexible liquid metal alloy (EGaIn) microstrip patch antenna," *IEEE Trans. Antennas Propag.*, vol. 60, no. 5, pp. 2151–2156, May 2012.



Brad L. Cumby (S'09) received the B.S. degree in electrical engineering from the University of Cincinnati, Cincinnati, OH, USA, in 2010, and is currently working toward the Ph.D. degree at the University of Cincinnati.

His research interests involve microfluidics and microfabrication of devices comprised of liquid metals, alloys, and alike.



David B. Mast received the B.S. degree in physics from Davidson College, Davidson, NC, USA, in 1973, the M.A. degree in physics from Wake Forest University, Winston-Salem, NC, USA, in 1975, and the Ph.D. degree in physics from Northwestern University, Evanston, IL, USA, in 1982.

From 1982 1984, he was a Post-Doctoral Research Associate with Case Western Reserve University. In 1984, he joined the Physics Department, University of Cincinnati, Cincinnati, OH, USA. His current research interests include the growth and characterization of carbon nanotubes; plasma treatment and surface functionalization of nanostructures including carbon nanotubes and nanofibers; microwave and millimeter-wave properties of advanced engineered and biological materials; microwave spectroscopy in medical physics and biophysics applications; and multi-functional nanoparticles for use in cancer detection and treatment.



Christopher E. Tabor received the B.S. degree in chemical physics from Centre College, Danville, KY, USA, in 2004, and the Ph.D. degree in physical chemistry from the Georgia Institute of Technology, Atlanta, GA, USA, in 2009.

From 2009 to 2010, he was a National Research Council Postdoctoral Fellow with the Air Force Research Laboratory. He is currently a Research Scientist with the Department of Defense, Materials and Manufacturing Directorate, Air Force Research Laboratory, Wright Patterson, OH, USA, where he is involved with optical and flexible materials research. His research interests include plasmonics, flexible electronics and optics, additive manufacturing, and RF photonics.



Michael D. Dickey (M'87) received the B.S. degree in chemical engineering from the Georgia Institute of Technology, Atlanta, GA, USA, in 1999, and the Ph.D. degree in chemical engineering from University of Texas, Austin, TX, USA, in 2006.

From 2006 to 2008, he was a Postdoctoral Fellow in the laboratory of Prof. George M. Whitesides at Harvard University. He is currently an Associate Professor of chemical and biomolecular engineering and a North Carolina State Faculty Scholar with North Carolina State University, Raleigh, NC, USA. His research interests include actuating and patterning soft materials including liquid metals, polymers, and gels.

Dr. Dickey was the recipient of the National Science Foundation (NSF) CAREER Award (2010), the Sigma Xi Faculty Research Award (2011), the Alcoa Foundation Engineering Research Award (2012), the Outstanding Teacher Award with Alumni Association Distinction (2012), and the SE-ASEE New Faculty Research Award (2013).



Jason C. Heikenfeld (S'98–M'01–SM'06) received the B.S. and Ph.D. degrees from the University of Cincinnati, Cincinnati, OH, USA, in 1998 and 2001, respectively.

From 2001 to 2005, he co-founded and served as Principal Scientist with the Extreme Photonix Corporation. In 2005, he returned to the University of Cincinnati, as a Professor with the Department of Electrical Engineering and Computing Systems. His university laboratory, The Novel Devices Laboratory (www.ece.uc.edu/devices), is currently engaged in electrofluidic device research for biosensors, beam steering, lab-on-chip, displays, and electronic paper. In addition to his scholarly work, he has led the creation of programs and coursework at the University of Cincinnati that foster innovation, entrepreneurship, and an understanding of the profound change that technology can have on society.

Dr. Heikenfeld is a Senior member of the Society for Information Display. He is a Member of the International Society for Optics and Photonics (SPIE) and the American Society for Engineering Education (ASEE). He is a Fellow of the National Academy of Inventors. He is an Air Force Office of Scientific Research (AFOSR) and Sigma Xi Young Investigator. He was the recipient of the National Science Foundation (NSF) CAREER Award.